Journal of Fluids and Structures 61 (2016) 168–183

Contents lists available at ScienceDirect

Journal of Fluids and Structures

journal homepage: www.elsevier.com/locate/jfs

Flow topology and unsteady features of the wake of a generic high-speed train

J.R. Bell [a,*], D. Burton [a], M.C. Thompson [a], A.H. Herbst [b], J. Sheridan [a]

[a] Department of Mechanical and Aerospace Engineering, Monash University, Clayton, Victoria 3800, Australia
[b] Centre of Competence for Aero- and Thermodynamics, Bombardier Transportation, Vasteras, Sweden

ARTICLE INFO

Article history:
Received 6 August 2015
Accepted 16 November 2015
Available online 23 December 2015

Keywords:
Streamwise vortices
High-speed train
Wake
Unsteady
Vortex shedding

ABSTRACT

The unsteady wake of a high-speed train is investigated experimentally. From a practical point of view, the wake region is of considerable importance as it is where slipstream velocities—velocities induced by the vehicles movement through air—are largest. In turn, this can create a considerable risk for passengers and track-side workers as the train passes. The flow is quantified in a 1:10 scale wind-tunnel experiment using high-frequency 4-hole dynamic pressure cobra probes, surface-pressure measurements and flow visualisation. The dominant feature of the time-average wake topology consists of a clearly identifiable counter-rotating streamwise vortex pair. Although the wake structure and evolution should perhaps be considered as a whole, the near wake exhibits periodic unsteadiness, at a Strouhal number of 0.2, that could be attributed to periodic shedding from the sides and to a lesser extent the top surface. This periodicity feeds into the trailing vortices, consistent with lateral and vertical displacement of the cores as they advect downstream and thus affecting maximum slipstream velocities.

1. Introduction

The geometry of modern high-speed trains (HSTs) is unique amongst ground-vehicles, having slender (length $\geq$ height), small aspect-ratio (width:height ratio ≈ 0.75) bodies, and a streamlined nose and tail with no fixed separation points. In general, the wake of a modern HST is expected to be a complex, unsteady, three-dimensional flow, consisting of shear layers, von Kármán-type vortex shedding, separation and recirculation regions, and a pair of counter-rotating streamwise trailing vortices (Morel, 1980; Weise et al., 2006; Muld et al., 2012; Bell et al., 2014). These vortices move downwards and outwards due to mutual induction and interaction with the ground as they advect downstream of the vehicle (Weise et al., 2006; Muld et al., 2012; Heine et al., 2013; Schulte-Werning et al., 2001; Yao et al., 2013; Bell et al., 2014). The vortices result from vorticity that is generated at, and advected along, the surface of the train, and then subsequently from the interaction between the downwash over the roof and tail of the train and the flow around the sides.

The wake of a HST is where the largest *slipstream* velocities are found to occur (Baker, 2010; Baker et al., 2012; Bell et al., 2014, 2015). Slipstream is the air flow induced by a vehicle's movement measured at a fixed distance from the vertical centreplane of the train. It is an important consideration for the aerodynamic performance but also for the safe operation of high-speed trains (HSTs). Such flows can be hazardous to commuters waiting at platforms and to track-side workers (Pope,

* Corresponding author.
E-mail address: james.bell@monash.edu (J.R. Bell).

http://dx.doi.org/10.1016/j.jfluidstructs.2015.11.009
0889-9746/

2007) due to significant induced pressure forces. Regulations are in place that limit the magnitude of slipstream velocities a HST can induce (European Rail Agency, 2008; CEN European Standard, 2009).

The authors have previously associated high slipstream velocities in the wake to the presence of a time-averaged streamwise vortex pair (Bell et al., 2014). The contribution of these vortices to characterising the slipstream of a HST has also been identified by preceding research (Baker, 2010; Weise et al., 2006; Muld et al., 2012). As the vortices move downwards and outwards beyond the passage of the train, the largest slipstream velocities are measured. The magnitude and location of the peak of instantaneous slipstream velocity in the wake has been shown to be inconsistent in scaled moving-model experiments (Baker, 2010; Bell et al., 2015) and numerical investigations (Muld et al., 2012; Pii et al., 2014; Hemida et al., 2014). Previous work by the authors has indicated this is caused by periodicity in the wake (Bell et al., 2015). Understanding the source of this high variation, and peak instantaneous slipstream velocities provides the potential for mitigation of the slipstream risk of HSTs, as well as improving stability and drag of the vehicle and the comfort of passengers.

A number of numerical researchers applying different methodologies and investigating various, albeit similarly modern, HST geometries have predicted that the streamwise vortex pair in the wake of HSTs exhibits spanwise oscillations. Delayed detached eddy simulations (DDES) of an Inter-City Express 2 (ICE2) HST by. Muld et al. (2012), using Proper Orthogonal Decomposition (POD) and Dynamic Mode Decomposition (DMD), identified a persistent streamwise vortex pair as the dominant wake feature, in contrast to a separation-dominated wake (Morel, 1980; Ahmed, 1983) seen with some generic automobile-like geometries. The dominant modes exhibited spanwise oscillations of the vortices occurring at a non-dimensionalized frequency, based on the freestream velocity and hydraulic diameter, of $St_{HD} = 0.085$, which they proposed to be caused by vortex shedding. Schulte-Werning et al. (2003) identified similar features on the same HST geometry in their unsteady simulations. Surface streamlines showed the point of origin of a pair of vortices oscillating in the spanwise direction around the vehicle's nose at $St_{HD} = 0.14$.

Numerical simulations using the Lattice Boltzman Method (LBM) by. Pii et al. (2014) identified vortex shedding at $St_W = 0.18$, developing from the underbody due to interaction with the bogies, before being released into the near wake. The near-wake exhibited spanwise fluctuations in velocity and pressure but the dynamics of the vortex pair was not presented. The results from a scaled wind-tunnel experiment on an ICE2 HST (Bell et al., 2014) indicates potential agreement with the unsteady numerical findings, although without confirmation of the flow structures responsible, as frequency and probability distribution analysis indicated periodicity at the location of the time-averaged vortex pair. Explicit experimental confirmation of the spanwise dynamics in the near-wake of a HST and the mechanism, which causes such movement, has not yet occurred.

The counter-rotating pair of streamwise wake vortices are typical of automotive ground-vehicles, as established by (Ahmed, 1983) and others (Vino et al., 2005; Krajnović and Davidson, 2005; Strachan et al., 2007), who also identified movement downwards and outwards from the symmetry plane as the fluid advects downstream. Coherent unsteady features of automotive wakes have been found by a number of researchers both experimentally and numerically (Lienhart and Pêgo, 2012; Vino et al., 2005). In addition to the time-averaged streamwise vortex pair in the wake of a 25° backlight-angle Ahmed body, researchers have identified signs of predominantly 2D von Kármán-type vortex shedding in the vertical plane. This occurs as the shear layers over the roof and under-body roll up, partially feeding the upper and lower recirculating regions, with the remainder rolling up to form the periodic sheet (Wang et al., 2013; Vino et al., 2005). A similar unsteady flow mechanism has been described by (Gilhome et al., 2001) for a notchback automotive geometry.

This work, part of a collaboration between Monash University and Bombardier Transportation, aids in the identification, description and quantification of the flow mechanisms responsible for the slipstream characteristics that affect the safety and operation of modern HSTs. Ultimately, it is hoped that the insight provided by this work will aid in the design of future generations of HSTs.

2. Methodology

2.1. Experimental model

A 1/10th-scale simplified version of a Deutsche Bahn Inter-City-Express 3 (ICE3) high-speed train is the model investigated in the presented work. The external shape, and thus external aerodynamics, are the same as the Siemens Velaro HST. This HST is in operation throughout Germany, Netherlands, Belgium, Austria, Switzerland, Denmark, France, Spain, Turkey, Russia, and China. The HST Computer-Aided Design (CAD) model geometry is freely available from the TC 256 Secretariat held by the DIN Standards Railway Committee (FSF)(DIN Standards Committee Railway, 2014). The availability of the ICE3 geometry, its wide use throughout the world, and its modern aerodynamic shape that is similar to other current HSTs in operation makes it an ideal geometry for studying the flow structures proposed to be typical of modern HSTs.

The ICE3 model measured $5.0 \times 0.3 \times 0.4\ \mathrm{m}^3$ ($L \times W \times H$), with a cross sectional area of $\approx 0.12\ \mathrm{m}^2$. The model had four sets of bogies, no pantographs, no inter-carriage gaps and no heating, ventilation and air conditioning (HVAC), as the essential geometry—the gross external shape—is the focus of this investigation. The model was supported by 6 pairs of 0.05 H (20 mm) diameter cylindrical supports in line with the wheels in the bogies.

2.2. Experimental setup

The setup models a train travelling on a straight track over flat ground with no crosswind. This approach aims to isolate the wake and resulting slipstream characteristics generated by the train's essential generic geometry in an ideal environment.

The experiment was performed in the Monash University 1.4 MW wind tunnel (Fig. 1). The wind tunnel is a closed circuit design, with fixed-pitch axial fans, driven by a 1.4 MW quad-motor system capable of wind speeds between 5 and 65 m/s.

The experimental setup in the wind tunnel and the coordinate system adopted are presented in Fig. 2. Streamwise position, x, is normalized by the model height (H), with $x=0$ corresponding to the position of the tail, as is the practice in general ground-vehicle aerodynamics (Bearman et al., 1988; Krajnović and Davidson, 2005). In addition, literature has indicated that the near-wake is dominated by the tail geometry (Morel, 1980; Muld et al., 2012). Cross-stream position, y, is normalized by the model width (W), with $y=-1/2$ corresponding to the left vertical edge and $y=1/2$ to the right edge. Vertical position, z, is normalized by model height, with $z=0$ corresponding to the top of the rails (TOR).

The 3/4 open test section measuring $12\times4\times2.5$ m^3($L\times W\times H$) was fitted with a 0.5 m (1.2 H) high splitter plane to reduce ground boundary layer effects, resulting in a cross-sectional area above the splitter plane of 8.0 m^2.

A 1/10th-scale *Single Track Ballast and Rail* (STBR) ground configuration (see Fig. 2b) was included in the setup, with height of 100 mm (0.24 H) and upper and lower widths of 300 mm (1 W) and 555 mm (1.85 W) respectively, adhering to the EN (CEN European Standard, 2009). The leading edge of the STBR had an front angle equivalent to the side angle (37°) swept 180 degrees. Velocity measurements established no separation occurred over the leading edge of the STBR.

The maximum blockage ratio was $\approx$ 2 % above the splitter plate, including blockage due to the traverse and STBR. Thus, blockage effects are expected to be minimal, and no blockage corrections were applied. The approximate turbulence intensity (I_{uvw}) above the wind tunnel boundary layer was 1.6 %.

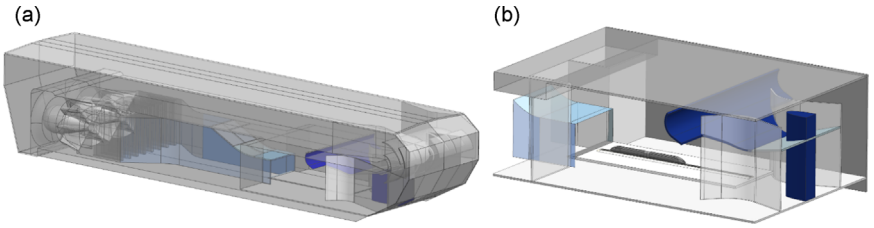

Fig. 1. (a) The Monash University 1.4 MW closed-return wind tunnel. (b) 1:10th-scale ICE3 model in the 3/4 open-jet test section. A 600 mm high splitter plate (shown) was utilised to reduce the ground boundary layer.

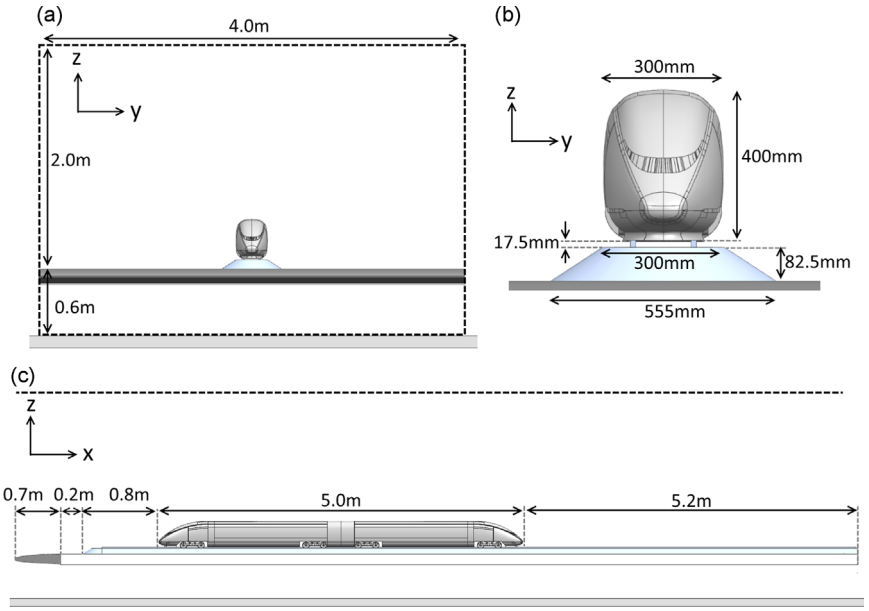

Fig. 2. The 1:10th-scale ICE3 model in the 3/4 open-jet test section of the Monash University 1.4MW wind tunnel. A 600 mm high splitter plate was utilised to reduce the ground boundary layer.

The reduced length-to-height ratio of $L/H = 12.5$, whereas full-scale HSTs operate at $L/H = 25-50$, is necessary to allow as large a scale model as possible in the test section, in order to achieve high Reynolds numbers. This is also a limitation of moving-model experiments for similar practical reasons. The high L/H of HSTs also presents a challenge numerically, as although technically they are not limited by physical space considerations, excessive computational resource requirements become an issue, with increased L/H coming at the cost of reduced Reynolds number and grid refinement. Although acknowledged in the literature (Weise et al., 2006), only recently has L/H been investigated by Muld et al. (2013); however, the effect of L/H has yet to be explicitly quantified.

Sensitivity of the results to Reynolds number over the range $Re_W = 0.5 \times 10^6 - 1 \times 10^6$, using width as the characteristic length, corresponding to freestream velocities of 25–48 m/s, is discussed in the results section, however this is still significantly smaller than the typical full-scale Reynolds number of 17×10^6 (corresponding to a full-scale train travelling at 300 km/h).

The authors acknowledge that the stationary floor is an experimental limitation. It results in a boundary layer that develops along the ground, which doesn't occur in full-scale HST operation. This is a common experimental limitation for wind tunnel experiments and can only be mitigated with difficult and costly solutions, such as boundary layer suction or a moving floor (rolling road). Kwon et al. (2001) highlight the difficulties of applying such solutions to HST experiments. The trains' long bodies means great care must be taken to apply the suction at multiple slot locations, noting that their position could influence drag measurements. Also, including a track and ballast shoulder ground configuration inhibits such a boundary layer treatment.

Another alternative to the wind-tunnel is to use a moving-model. Such experiments have been performed to measure the velocity or pressure beyond the path of the train (Baker, 2010; Bell et al., 2015; Gilbert et al., 2013). The moving-model ensures the correct relative motion between the ground and the model, thus no ground boundary layer develops. However, flow mapping in the near wake of the vehicle becomes difficult and has only recently been shown possible using high speed Particle Image Velocimetry (PIV) by Heine et al. (2013).

The flow structures of most interest to the current research, the pair of streamwise vortices in the near-wake, has been found to be largely insensitive to a stationary floor in experiments by Strachan et al. (2007) and in a numerical investigation by (Krajnović and Davidson, 2005). As the model is also situated above a scaled ballast and rail, the distance between the model and the developing ground boundary layer is increased. It has been proposed that this potentially reduces the effect of the stationary floor (Schober et al., 2010) at least for the reduced-length model adopted here. Thus the results presented are proposed to represent the flow around a full-scale HST. However, possible influences of the stationary floor on the results is discussed in individual sections.

The measured displacement thickness of the boundary layer was $\delta^*/H = 0.006$ and 0.035 at the model's nose and tail positions, respectively, in an empty tunnel above the splitter plate.

The boundary layer over a HST has been shown to be highly three dimensional (Baker, 2010), with the side boundary layer being sensitive to distance above the ground. Thus the side and roof boundary layers were measured and analysed as 2D boundary layers for simplicity as previous researchers have done (Baker, 2010; Muld et al., 2013). The displacement thicknesses of the boundary layer at $x = -2.5$ at the side, and $z = 0.5$ on the roof, both at $y = 0$, were $\delta^*/H = 3.12 \times 10^{-2}$ and 2.82×10^{-3}, respectively. These correspond to momentum thicknesses of $\theta/H = 2.50 \times 10^{-2}$ and 2.70×10^{-3} for the sides and roof, respectively.

2.3. 4-Hole cobra probe measurements

Measurements were taken with a 4-hole dynamic-pressure probe (cobra probe). Specifications indicate that the cobra probe is capable of determining velocities with the accuracy of $\pm$ 1 m/s within a $\pm 45^\circ$ cone angle; however, it is not capable of measuring reversed flow (Hooper and Musgrove, 1997). Despite this, an indication of the percentage of flow that is outside its calibrated cone of acceptance is provided by the probes accompanying software, and in all cases reported $>95\%$ of measurements were within the cone of acceptance.

Measurements were taken in spanwise (yz) planes at $x = 0.5, 1, 2, 3, 5, 6$, on a square grid of $\Delta y, \Delta z \approx 0.05$. Measurements were performed in both the positive and negative y domain to confirm centerplane reflection symmetry of the flow, with only a half plane presented. Two cobra probes mounted with 0.25 (100 mm) spacing were positioned using an automated traverse. These measurements had a sample time of 15 s. The cobra probes were also fixed at individual points, in which case 60 s samples were obtained.

The velocities measured by the cobra probe in the wind tunnel have a train-fixed (TF) frame-of-reference. The component of the velocity in the x direction (u) was converted to the ground-fixed (GF) frame-of-reference, the perspective of a stationary observer who experiences slipstream, and normalized against the freestream velocity:

$$u_{GF} = 1 - \frac{u_{TF}}{u_\infty}. \tag{1}$$

The reference velocity, u_∞, was calculated from an upstream reference pitot-static tube, corrected to the model's position through a dynamic-pressure correction factor.

The cobra probe, consisting of the set of tubes and four differential pressure transducers, is specified by the manufacturer (TFI) to have a frequency response above 2000 Hz.

2.4. Tail surface pressure

The tail of the model was fitted with 120 surface pressure taps over one half and a single pressure tap on the other. The taps were connected by PVC tubing to differential pressure transducers of a 128-channel Dynamic Pressure Measurement System (DPMS). A higher concentration of the taps was located at the end of the tail, based on expected flow topology (Fig. 8(a).

In such systems, phase and amplitude of the pressure measured by the transducer is distorted from the true pressure at the desired measurement point due to resonant characteristics of the tube (Iberall, 1950). The amplitude and phase response for each measurement was corrected using the *inverse transfer function* (ITF) method (Irwin et al., 1979) with the frequency response of the pressure measurement system being determined theoretically (Bergh and Tijdeman, 1965). This method of correction is common for dynamic pressure measurements obtained in applied aerodynamics research, see for example (Vino et al., 2005; Gilhome et al., 2001). Irwin et al. (1979) has shown through experiments that the ITF method reduces the average magnitude of error between true and measured pressure from 9.6% and 27.4% to 1.6% and 4.1% for tubing systems of 0.6 m and 3 m in length, respectively—covering the range of tube lengths utilized in this study.

The frequency of the primary peak in the amplitude response, and the frequency where the amplitude response is below 0.4, are two important characteristic frequencies of the uncorrected frequency response. The primary peak in amplitude occurred at St_W=0.36 (42 Hz) and the amplitude response fell below 0.4 at St_W=6.9 (810 Hz). The dominant frequencies were expected to lie within the range St_W=0.1–0.25 from existing literature (Pii et al., 2014; Muld et al., 2012; Schulte-Werning et al., 2003), corresponding to frequencies in the range of 10–50 Hz, thus the frequency response of the surface-pressure measurement system is suitable for the range of frequencies of interest.

The sampling frequency was limited to f_s=1000 Hz to prevent overloading the data acquisition system, due to high bandwidth generated from multiple simultaneous channels. This sampling rate in the 1/10th-scale experiments with freestream velocities of 25–45 m/s corresponds to 333–185 Hz for a full-scale, operational HST travelling at 300 km/h. Sampling times of 60 s were used.

The actual pressures measured by equipment, P_i, were converted to pressure coefficients using total, P_t, and static, P_s, pressure, from an upstream reference pitot-static tube:

$$C_P = \frac{P_i - P_s}{P_t - P_s}. \tag{2}$$

3. Results

3.1. Time-averaged wake structure: mean cobra-probe measurements

The time-averaged flow characterisation indicates an association of high slipstream velocity to a pair of streamwise counter-rotating vortices.

Regions of high streamwise induced velocity, u and high $\sqrt{u^2+v^2+w^2}+\sigma_{uvw}$, a statistical measure of the largest velocities a stationary observer would likely experience, are shown in Fig. 3(a) and (Fig. 3(b) respectively. Here, the standard deviation, σ_{uvw}, is the square root of the sum of the variances of the velocity components. These regions are shown to spread downwards and outwards as they move downstream. These regions are caused by the time-averaged vortex that also moves downwards and outwards as it moves downstream. The vortex is identified by the spanwise and transverse velocity components (v,w), and the vorticity in the yz plane (ω_x), as well as the vortex identifiers: Γ_1 and Γ_2 (Graftieaux et al., 2001; Jeong and Hussain, 1995). The vortex boundary is defined as $\Gamma_2 = 2/\pi$, and its core by the maximum of Γ_1.

This lateral movement of these counter-rotating longitudinal vortices is consistent with inviscid flow theory, where no flow through the ground can be represented by mirror images of each of the vortices. The self induction of the vortex pair and interaction with the image pair causes the pair to move initially towards the ground and then away from each other. As the pair approach the ground, some level of flattening of the cores occurs (Westphal and Mehta, 1989; Pauley and Eaton, 1988; Lödgberg et al., 2009) as is the case in the results presented. It is the no-slip condition in the spanwise direction that causes this lateral movement, while the no-slip condition in the streamwise direction, from the artificially imposed stationary floor, is not expected to influence this lateral motion significantly.

Although the boundary layer clearly does not dominate these measurements, the presence of the stationary floor presents a different flow condition and the wake structure is expected to show some differences to a moving floor or moving-model setup. Stationary floor results are expected to show a flatter overall wake structure. This has been seen in longitudinal vortices embedded in or moving towards a boundary layer (Westphal and Mehta, 1989; Pauley and Eaton, 1988; Lödgberg et al., 2009). The distortion of the ground boundary layer by a vortex leads to rapid diffusion of streamwise vorticity, resulting in a larger vortex core (Pauley and Eaton, 1988), also leading to an increase in the flattening of the vortex core (Westphal and Mehta, 1989; Lödgberg et al., 2009).

A number of researchers have found that a pair of counter-rotating longitudinal vortices analogous to those in the HST wake, which develop over the C-pillar of generic automotive vehicles, are largely insensitive to the stationary floor in the near wake. Large Eddy Simulations (LES) of (Krajnović and Davidson, 2005) at a Reynolds number of 2×10^5 indicated the

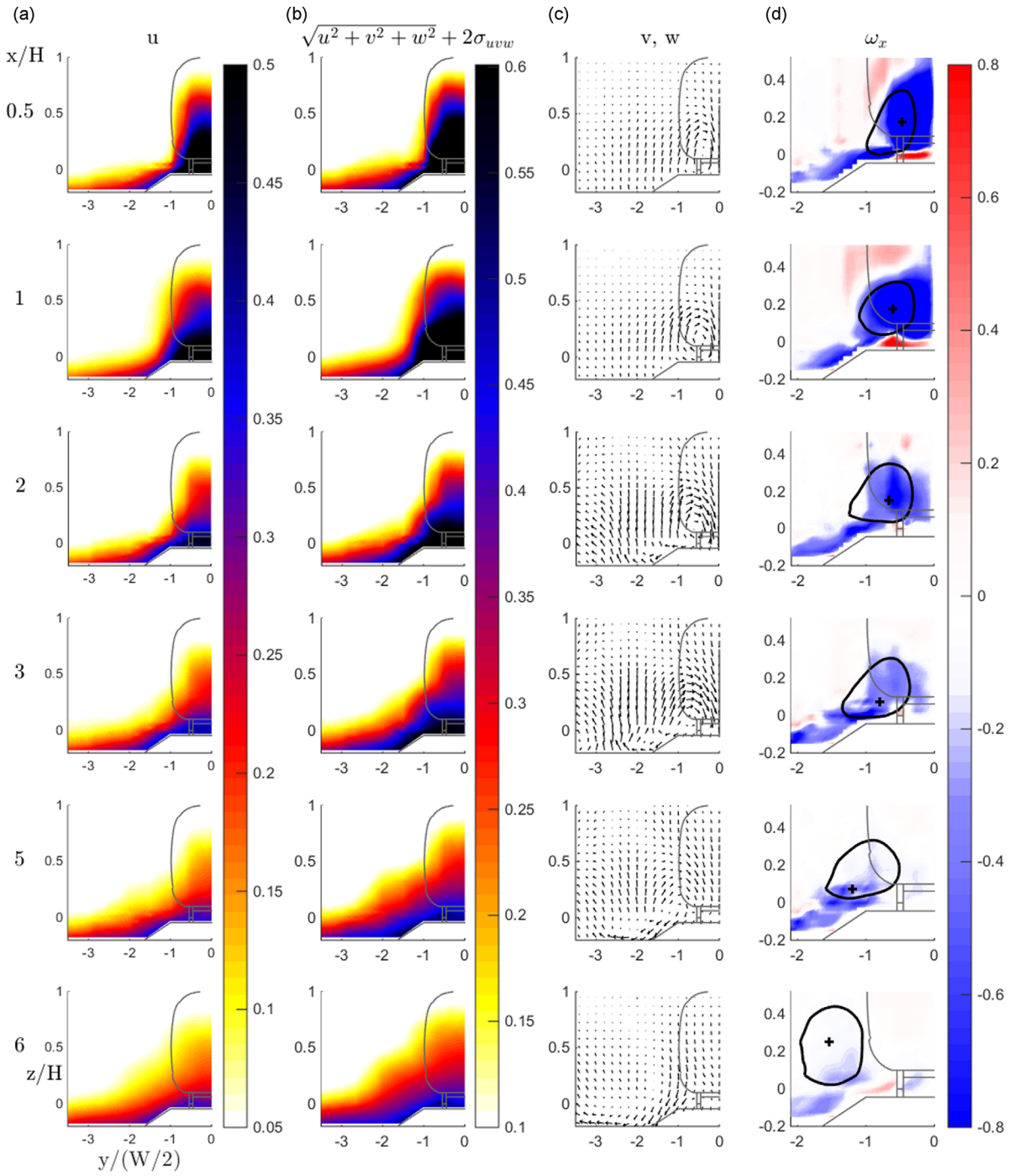

Fig. 3. (a) $\overline{u}$, (b) $\sqrt{\overline{u^2}+\overline{v^2}+\overline{w^2}}+\sigma_{uvw}$, (c) $\overline{v},\overline{w}$ vectors, (d) Streamwise vorticity colormap of ω_x, Contour lines of $\Gamma_2 = 2/\pi$, with + indicating the position of max $[\Gamma_1]$.

stationary floor influenced the base pressure. Despite this, velocity profiles close to the ground and at a number of streamwise locations displayed only minor differences between a moving and stationary floor, leading the authors to conclude the longitudinal vortices were relatively insensitive to ground effect. The scaled experiments by Bearman et al. (1988) presented velocity profiles from pulsed-wire anemometry together with drag and lift measurements that indicate the effect of a moving floor was negligible for a Davis generic automotive model with zero upsweep angle. Similarly, Strachan et al. (2007) noted the C-pillar vortices of an Ahmed body were insensitive to the motion of the floor in their scaled

experiments at a Reynolds number of 1.7×10^6 with a rolling road, based on velocity profiles obtained from Laser Doppler Anemometry (LDA).

The link of the high slipstream velocities in the wake to the streamwise vortices have previously been demonstrated by the authors in Bell et al. (2014). Importantly, the wake structure identified by the numerical investigations (Hemida et al., 2014; Muld et al., 2012; Yao et al., 2013) which modelled a moving-floor, and in particular the moving-model experiments by Heine et al. (2013) is qualitatively similar to that presented here. Further, the good agreement of streamwise velocity profiles in the wake between full-scale measurements and scaled moving-model (Bell et al., 2015; Baker et al., 2001) and numerical (Hemida et al., 2014; Muld et al., 2012) results with reduced Reynolds numbers indicate Reynolds number does not result in a significant change in the wake structure. Thus, the flow topology identified is proposed to be representative of full-scale flow around a HST.

3.2. Unsteady wake structure

3.2.1. Flow turbulence, wake structure and periodicity

Data obtained from the cobra probe measurements are analysed in this section to quantify the unsteadiness in the wake. As is revealed through the spectral analysis discussed later, the *turbulence* levels discussed in this section consist of coherent periodic oscillations of the mean wake together with true turbulent fluctuations.

The turbulent intensity in all three components of velocity measured in the *yz* planes by the cobra probes are presented in Fig. 4. These measurements show that the turbulence in the wake is not isotropic.

The streamwise turbulence intensity (I_{uu}) is clearly associated with the time-averaged streamwise vortex identified in Fig. 3.

The spanwise turbulence intensity (I_{vv}) also shows an association with the streamwise vortex, with levels of $I_{vv} \approx 8\%$ matching the movement of the structure. However, as is most evident at $x=1$ and 3, high levels of spanwise turbulence also exists in a spanwise band centered at $y=0$ at a height of $z=0.2$. At these x positions, the streamwise vortex has moved outwards beyond the centreline. A possible explanation for this is von Kármán-type vortex shedding occurring in the *xy* plane; this is explored below.

Close to the rear of the train, the vertical turbulence intensity, I_{ww}, appears to be associated with a third unsteady feature, one much closer to the centreplane, with much lower direct association with the streamwise vortex. A potential flow mechanism for this is vertical shedding in the *xz* plane, as identified behind automotive vehicles in previous studies (Vino et al., 2005; Gilhome et al., 2001; Wang et al., 2013; Minguez et al., 2008).

The same domains and contour ranges are used for all plots in Fig. 4, this highlights that the streamwise fluctuations are largest and they remain high in the streamwise vortex core further into the wake (max $\approx 11\%$ at $x = 6\,H$). In comparison, the spanwise turbulence is similar but at a lower intensity (max $\approx 8\%$), while the vertical intensity is much lower (max $\approx 5\%$).

Spectral analysis was performed on all pointwise cobra probe measurements, both those from traversing *yz* planes, and from those individually mounted. The specific positions are presented in Fig. 6. The corresponding results are shown in Fig. 7. A Fast Fourier Transform (FFT) routine was utilized to convert the time sequences to the frequency domain.

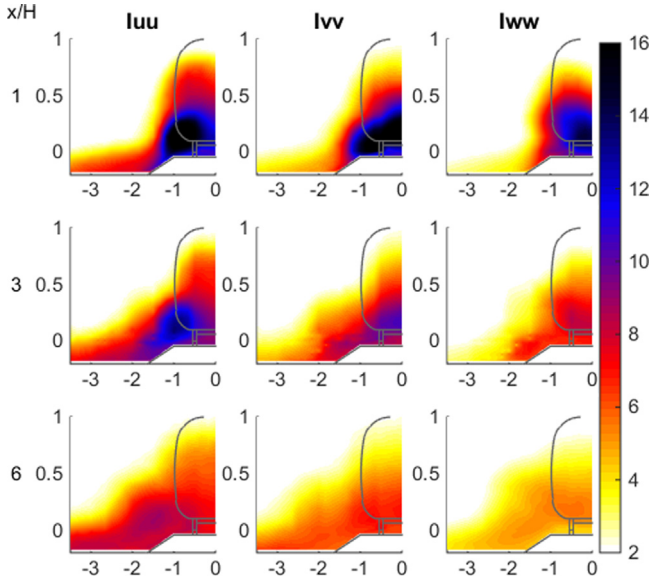

Fig. 4. Turbulence intensities of the three velocity components: $\sigma_u/U_\infty, \sigma_v/U_\infty, \sigma_w/U_\infty$, in the *yz* plane at $x=1$, 3, 6, from cobra probe measurements.

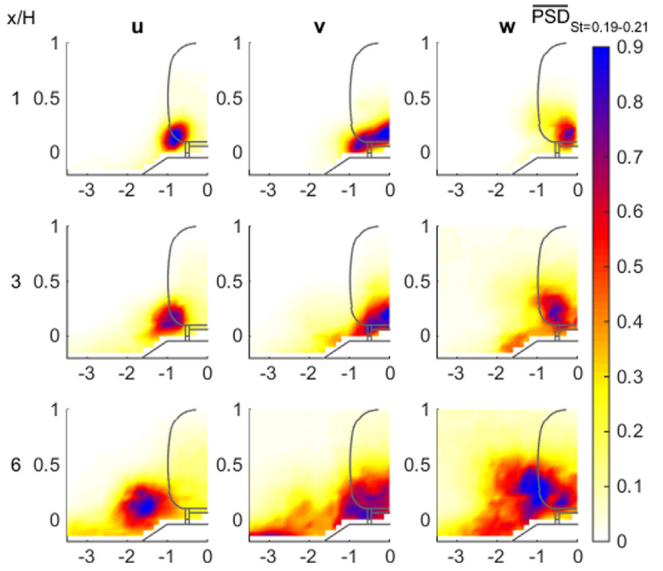

Fig. 5. Magnitude of PSD for (u, v, w) components over the frequency band St_w=0.19–0.21 in the yz plane at x=1, 3, 6. Data from cobra probe measurements.

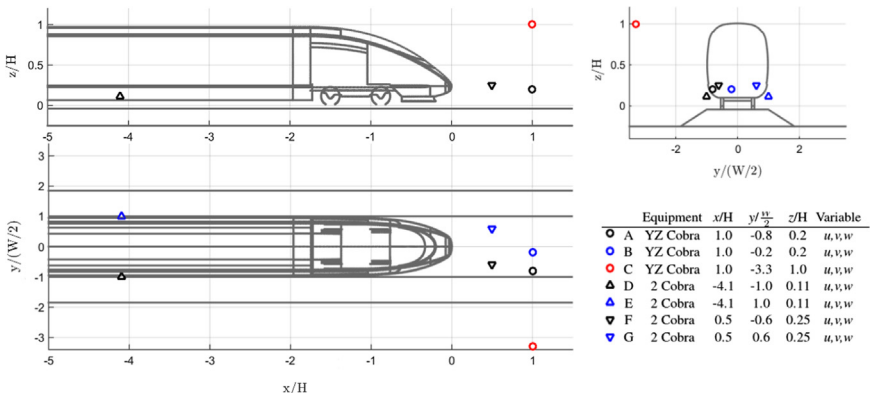

Fig. 6. Spatial positions of the cobra probes traversed in the yz plane and individually mounted.

The Hamming window methodology was applied using 16 windows with 50% overlap. The average of the multiple windows was then taken, in an attempt to reduce spectral leakage.

A dominant frequency was identified in the Power Spectral Density (PSD) to occur at St_W=0.2 in the regions of high turbulence intensity for all three velocity components measured by both measurement setups (Fig. 7). This Strouhal number was consistent across Reynolds numbers tested ($Re_W = 0.5 \times 10^6 - 1 \times 10^6$). This Strouhal number is consistent with von Kármán-type vortex shedding occurring behind fundamental bluff bodies such as cylinders. However, areas of peak power spectral density varied between the three velocity components, in the same manner as found for the turbulence intensity plots in Fig. 4.

Measurements made by the cobra probes traversed through the yz planes that exhibited this St_W=0.2 dominant frequency are represented spatially for each velocity component in Fig. 5. This is done by presenting the average PSD over the range of St_W=0.19–0.21, $\overline{PSD}_{0.19-0.21}$, as a filled contour.

The high $\overline{PSD}_{0.19-0.21}$ of the u component is clearly directly associated with the streamwise vortex core. The v component has medium levels of $\overline{PSD}_{0.19-0.21}$ in the vortex core, yet higher $\overline{PSD}_{0.19-0.21}$ in a spanwise band centred at y=0 at a height of z=0. This is also visible in Fig. 4, however it is clearer in these results. These results support the argument that at least some degree of spanwise vortex shedding is occurring, contributing to the dominant frequency of St_W=0.2. As the streamwise velocity component in the vortex core also exhibits periodic fluctuations at the same frequency, it is proposed that the oscillation of the trailing vortex pair is controlled by or locked to the near-wake spanwise oscillation.

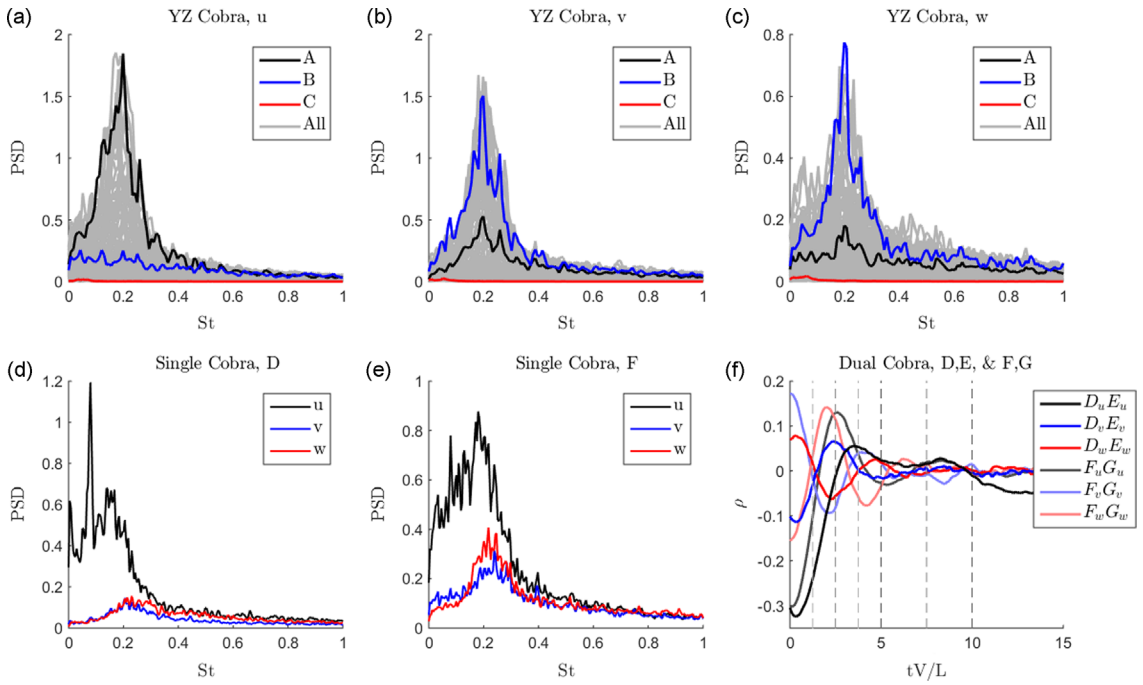

Fig. 7. Power spectral density of cobra probe velocity signals for traversed probes (a) u, (b) v, (c) w, and individual cobra probes at (d) position D and (e) position F. (f) Cross-correlation of dual cobra probe measurements at position D and E, and F and G. Positions A-G presented in Fig. 6.

The $\overline{PSD}_{0.19-0.21}$ for the w component is also similar to the corresponding turbulence results in Fig. 4, with high $\overline{PSD}_{0.19-0.21}$ starting in the centre of the model and slowly moving outwards, yet still remaining inward of the streamwise vortex.

The proposal of spanwise oscillation (vortex shedding) controlling the oscillation of trailing streamwise vortices as they advect downstream from their source has not been established previously in the literature to the knowledge of the authors. It is possible that the small aspect ratio of the HST contributes to this, being $AR = W/H \approx 0.75$ compared with a standard Ahmed body ($W/H = 1.75$). The significance for HST geometry is that the sides are closer together than the roof and base, whereas for a ground vehicle the opposite is true. Notably (significant) spanwise shedding has not been identified in automotive wakes, while vertical shedding has (Vino et al., 2005; Gilhome et al., 2001; Wang et al., 2013; Minguez et al., 2008). Additionally, a HST generally has smaller ground clearance, reducing the similarity in flow over and under the body. Further, a HST typically has a more three-dimensional nose/tail—due to greater side taper—whereas automotive vehicles more commonly have smaller side taper, and therefore a more pronounced two-dimensional rear shape, as represented in the idealised case of the Ahmed body. This streamlining means that modern HSTs in general exhibit a far smaller separation region at the tail. A consequence of this, is that although the turbulence and frequency results suggest some degree of shedding in the vertical plane from the roof and underbody, this is expected to be significantly weaker than for automobile geometries.

These results have experimentally confirmed the periodicity of the streamwise vortices, as predicted by numerical researchers, at a higher level of detail than the authors have done previously in Bell et al. (2014) where only point-wise frequency analysis was presented. The Reynolds number of these experiments ($\mathrm{Re}_W = 0.5 \times 10^6 - -1 \times 10^6$) are larger than the moving-model ($\mathrm{Re}_W = 3.3 \times 10^5$ (Bell et al., 2015; Heine et al., 2013)) and numerical research ($\mathrm{Re}_W = 6 \times 10^4$ (Muld et al., 2012)) previously undertaken. Also, for the first time, the causes of the periodicity in the streamwise vortices have been proposed; vortex shedding off the sides and weaker shedding off the roof, based directly on analysis of the unsteady results presented.

The PSD and cross-correlation of two simultaneous cobra probe measurements located upstream, either side of the body, and separately, in the near wake either side of the xz symmetry plane are also presented in Fig. 7(d,e,f).

Both positions exhibit a broad peak in PSD around the frequency of St_W=0.2, although this is clearer for the v and w components. However, at the sides upstream of the tail a sharp peak is also evident at St_W=0.06 in the u component.

The cross-correlation of the velocities measured by the two sets of probes symmetrically placed on opposite sides of the wake show a relatively high level ($\rho_{\pm y} = 0.30$) of correlation for u , but 180° out-of-phase at both positions. A lower level ($\rho_{\pm y} = 0.15$) of correlation, 180° out-of-phase is also visible for the v and w components for the upstream and downstream positions, respectively. In contrast, a similar level ($\rho_{\pm y} = 0.1$) of in-phase correlation, is visible for the w and v velocity components for the upstream and downstream positions, respectively. An explanation for the switching of the phase of secondary components from upstream to downstream is through the changing flow topology around the HST tail, the 3D

geometry alters the predominantly-streamwise incoming flow into a combination of streamwise, spanwise and transverse flow, most notably as the streamwise vortices.

The out-of-phase u-component cross-correlation from dual cobra probes in the near wake together with the in-phase v cross-correlation further supports the conjecture of spanwise vortex shedding contributing to the near-wake structure. This is consistent with the effect that alternatively shed vortices would have on the u and v components.

These frequency spectra from the upstream points situated at the sides of the train close to ground level indicate that the periodicity observed in the wake can also be observed a considerable distance upstream. Whether the upstream periodicity along the side surfaces of the train is being amplified to cause large wake fluctuations downstream, as suggested by Pii et al. (2014), or it is just a weak upstream response to downstream periodicity, cannot be determined from these results. It is well established that von Kármán-type vortex shedding occurs behind (predominately two-dimensional) bluff bodies without upstream interference triggering the phenomenon (Provansal et al., 1987), which is caused by an absolute instability of the wake recirculation region. However, periodic fluctuations upstream, as a causal mechanism for the downstream fluctuations, would infer communication between the sides of the vehicle. This is proposed by Pii et al. (2014) through vortex shedding occurring around the bogies in the underbody. However, such communication is expected to be difficult due to the low flow rates underbody, particularly in this experiment with a stationary floor.

Periodicity in the wake of a HST has been observed irrespective of whether the ground was stationary or moving (Muld et al., 2013, 2012; Schulte-Werning et al., 2003; Pii et al., 2014; Bell et al., 2014). The Large Eddy Simulations of (Krajnović and Davidson, 2005) predicted a stationary floor reduced the clarity of dominant frequencies found in the transient flow compared to that seen for a moving floor. However, a clear dominant frequency was observed in both the flow mapping and surface pressure in the experimental results presented here. A significant difference exists between the dominant frequency found in these results, $St_W = 0.2$, and that of the other researchers: $St_{HD} = 0.085$ by Muld et al. (2012), $St_{HD} = 0.14$ by Schulte-Werning et al. (2003), $St_W = 0.18$ by Pii et al., 2014 and $St_W = 0.18$ by Bell et al. (2014). Muld et al. (2013) predicted that the length of the train modelled influenced the dominant frequency, where trains of $L/H = 12.5, 19, 25$ exhibited dominant frequencies of $St_{HD} = 0.13, 0.095$ and 0.085, respectively. An explanation for this influence, as well as the variation in dominant frequencies found by other researchers, could be in the difference in boundary layer development and corresponding displacement thickness. Similarly, a difference in the Reynolds number is also expected to affect the boundary layer development over the train. The different length or Reynolds number would result in a different 'effective' characteristic length (width, hydraulic diameter, frontal area). Basing the Strouhal number on this variable length scale (e.g., the physical width plus boundary layer widths (Roshko, 1955)) rather than the actual train width may allow a collapse of the results from the different research groups. Unfortunately the boundary layer thickness data required to test this hypothesis is not available.

3.3. Tail surface pressure

The time-average and standard deviation of the tail surface pressure data are presented in Fig. 8(a) and (b) respectively. A band of low pressure is visible over the roof and around the sides of the vehicle. This is attributed to the acceleration of the flow around the curved surfaces of the roof and sides. Over the wind-screen there is a region of higher pressure where the flow remains attached to the surface. This adverse pressure gradient along the surface leads to bulk flow separation at the tip of the tail. Minor flow separation and subsequent reattachment occurs at the wiper housing geometry, tapered halfway down the windscreen. A small region of high pressure is visible in front of this feature.

The presence of the streamwise vortex is not identifiable in the time-averaged pressure distribution in Fig. 8(a), however the peak in standard deviation on the corner near the tail tip is likely related to these unsteady structures (Fig. 8(b).

Spectral analysis of a number of key points on the surface Fig. 8(d), selected based on standard deviation levels in 8(b), are presented in Fig. 8(e). These key points are near tip of the tail, in the region of high standard deviation at the tail corner, in the separate region of high standard deviation along the tail side, and the roof and side upstream of the tail. The dominant frequency of St_W=0.2 is clear on the side of the tail, and present at the corner edge Fig. 8(e), however, it exists in a broader peak than found with the wake measurements (Fig. 7). The tail tip, where flow is expected to have separated, and pressure at both the roof and side upstream of the tail show no dominant frequencies. The average PSD magnitude over the range $0.19 < St_W < 0.21$ is presented in Fig. 8(c). This region of high PSD with a dominant frequency St_W=0.2 accounts for the regions of high standard deviation. Once again, these results provide signs of the periodic features occurring on the tail surface at the same frequency as in the wake.

The cross-correlation of two taps located at the same position, either side of the vehicle, is presented in Fig. 8(f). The pressure either side of the vehicle is 180 ° out-of-phase, however, the level of correlation of 0.15 is relatively low. The non-dimensional time period, $tv/L = 5$, corresponds to a periodicity of St_W=0.2.

The surface pressure distribution over the tail compares well to surface flow visualisations presented in Fig. 9. The attached flow over the roof and windscreen, as well as around the majority of the side surfaces is evident. Separation at the tail tip is also evident, however the surface visualisations show regions of separation up the two corners of the tail. Smoke visualisation and wool tufts—not presented here—identified these regions as the roll-up location of the streamwise vortex pair. Thus, these regions of separation are attributed to the pair of streamwise vortices.

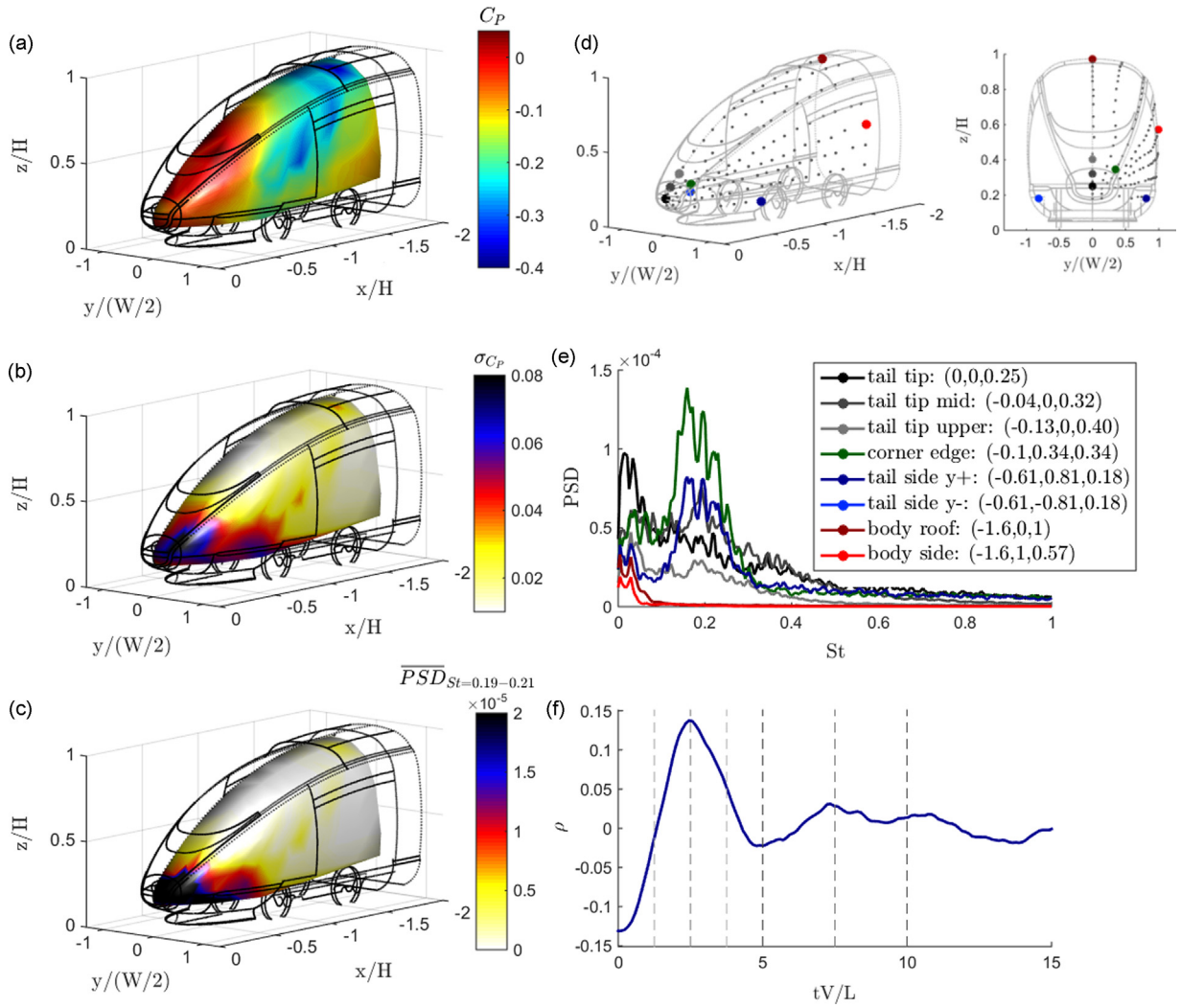

Fig. 8. (a) Time-averaged surface pressure, $\overline{C}_P$. (b) Standard deviation of surface pressure, σ_{C_P}. (c) Average magnitude of PSD between $0.19 < St_w < 0.21$. (d) Locations of selected points on the surface, (e) PSD of pressure at selected points, (f) Cross-correlation of points either side of tail at $x = -0.61$ H, $y = \pm 0.81(W/2), z = 0.18$ H.

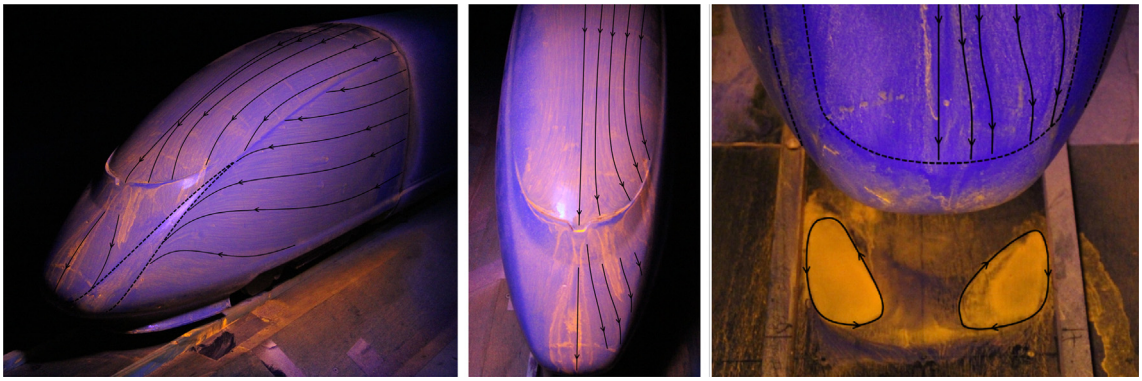

Fig. 9. Annotated surface flow visualisation over the tail of the ICE3 HST.

3.3.1. *Surface-flow visualisations*

Surface flow-visualisation on the ballast near the tails tip identify the signs of an arch vortex approaching the ground (Fig. 9). This is the same mean-flow structure found behind surface-mounted cubes (Castro and Robins, 1997) with

similarities to separation regions behind automotive vehicles (Vino et al., 2005; Wang et al., 2013; Gilhome et al., 2001; Minguez et al., 2008). This type of structure has previously been identified in the unsteady wake of a notch-back automotive vehicle by Gilhome et al. (2001).

The reduced flow under the train caused by the HST geometry is expected to be further reduced by the stationary floor. This flow is consistent with the arch vortex approaching the ground, rather than forming a toroidal vortex, which would be expected in a more symmetrical geometry and a moving floor. The difference in flow topology, and corresponding surface pressure, between a stationary and moving floor would be expected to be most significant on the underbody. Automotive vehicles with rear diffusers have been found to be most susceptible to the influence of floor motion (Bearman et al., 1988). However, the ICE3 HST model does not have a diffuser-type geometry, due to the presence of an underbody spoiler and is therefore expected to be less sensitive to the ground effect. This has been seen in scaled wind tunnel experiments of a generic automotive vehicle by Heft et al. (2012), who identified the surface pressure over the roof and around the sides of the vehicle to be largely insensitive to the presence of a moving or stationary ground.

3.3.2. Time-averaged topology

The time-average wake flow topology determined from the wake cobra-probe measurements, and its origins on the tail surface, from surface pressure and flow visualisations, is presented in Fig. 10(a).

The vorticity that is present in the wake of the HST is generated through the tangential pressure gradients on its surface (Morton, 1984, 1987). The advection of vorticity from the surface into the wake can be described by vortex filaments, derived from Helmholtz's vortex theorems where vorticity is constant along the length of a filament and a filament must extend to a boundary or form a closed loop. The accelerating and decelerating regions of tail surface pressure and separation regions identified in the surface flow visualisations inform the motion of vortex filaments, illustrated in Fig. 10(b). The vorticity that develops over the surface of the vehicle gradually turns from being in the vertical plane, ω_y, over the roof and the spanwise plane, ω_z, at the sides, due to the decelerating region over the tail tip approaching separation, into the streamwise plane, ω_x, in two opposing directions. Once advected off the surface of the HST, this tilted vorticity feeds the streamwise vortex pair.

However, not all vorticity is turned into the streamwise direction. Vorticity in the spanwise plane, ω_z, is advected off the sides of the vehicle, below where the streamwise vortices roll up. This is also visible in Fig. 9 where attached flow can be seen to pass underneath the separation lines. Additionally, some vorticity in the vertical plane, ω_y is also advected from the tail tip and underbody.

3.3.3. Transient flow topology

The transient surface pressure is presented in Fig. 11(a) as fluctuating pressure over 5 instantaneous time-steps in series, from data with a single-pole $0.08 < St_W < 0.45$ bandpass-filter applied. Alternating regions of high and low fluctuations around the average pressure translate along the tail side to the tip.

The data from the surface pressure measurements was phase-averaged using a single cobra probe, located at $x = 0.5(H), y = 0.55(W/2), z = 0.25(H)$, positioned in the core of one of the time-averaged streamwise vortices, and used as a control signal. Again, a single-pole $0.19 < St_W < 0.21$ bandpass Butterworth filter, based on the observed dominant frequency of St_W=0.2, was applied to the control signal, as well as the corresponding surface pressure data. These results (see Fig. 11(b) represent the instantaneous time-steps well, again exhibiting alternating regions of high and low deviations in pressure, presented as the difference between phase-averaged pressure and time-average pressure:

$$\Delta C_P = C_{P,\phi = i^o} - \overline{C}_P. \tag{3}$$

These alternating regions of pressure translate along the tail side to the tip. This implies that the pressure fluctuations on the tail surface are associated with the pressure fluctuations in the near wake of the HST. As discussed above in Section 3.2

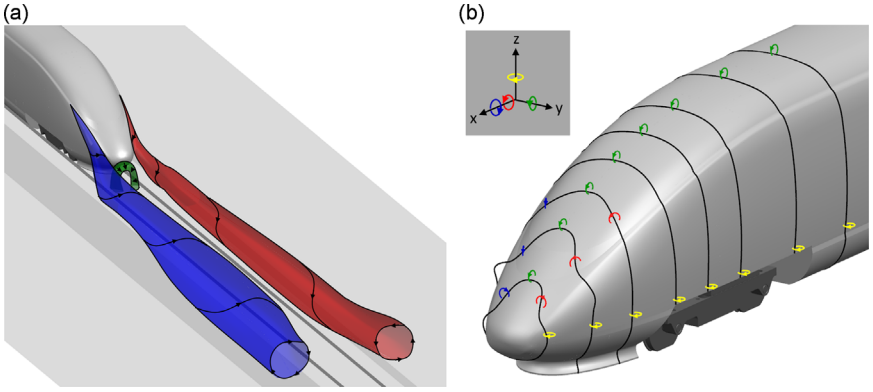

Fig. 10. (a) Time-averaged wake topology, b) Predicted advecting vortex filaments over the tail of the ICE HST.

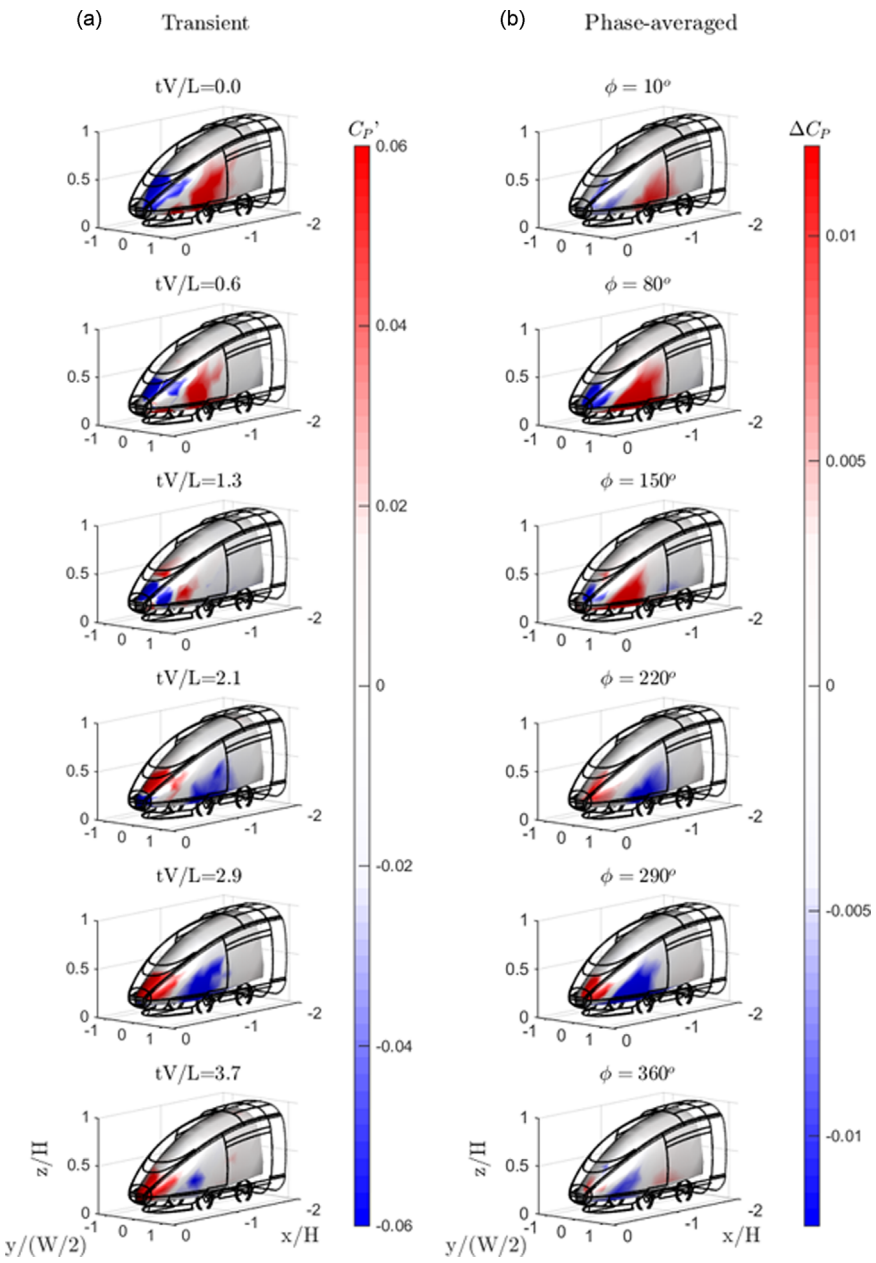

Fig. 11. (a) A series of instantaneous snapshots of $0.08 < St_w 0 < 0.45$ bandpass-filtered fluctuating surface pressure, C_p', on model tail. $tV/L = 0$, 0.6, 1.3, 2.1, 2.9, 3.7. (b) Phase-averaged fluctuating surface pressure, C_p', on model tail. Phase angles, $\Phi = 10$, 80, 150, 220, 290, 360° presented.

regarding the dual cobra probes upstream, this phenomenon is proposed to be due to pressure fluctuations feeding forward upstream along the train surface.

3.3.4. *Proper orthogonal decomposition*

The transient pressure data was further analysed using Proper Orthogonal Decomposition (POD) (Lumley et al., 1967) in the manner of Sirovich's snapshot method (Sirovich, 1987). POD has been used extensively in fluid dynamics research by Graftieaux et al. (2001); Perrin et al. (2007); Muld et al. (2012), and more recently in the wake of HST's (Muld et al., 2012).

The three dominant modes are observed in Fig. 12(a, b, c). The first fluctuating mode, Mode 1, accounts for 35% (Fig. 12d) of the total fluctuating pressure. Mode 1 represents a region of increase/decrease of pressure at the tail corner, the same region of high standard deviation and PSD at $St_W = 0.2$ (Fig. 8). Mode 2 has a lower contribution of 11% and identifies two alternating regions of increase/decrease in surface pressure, one just inside of the tail corner, the other at the tail side. These two modes are proposed to be associated to the origins of the spanwise vortex shedding. Mode 3 has similar level of

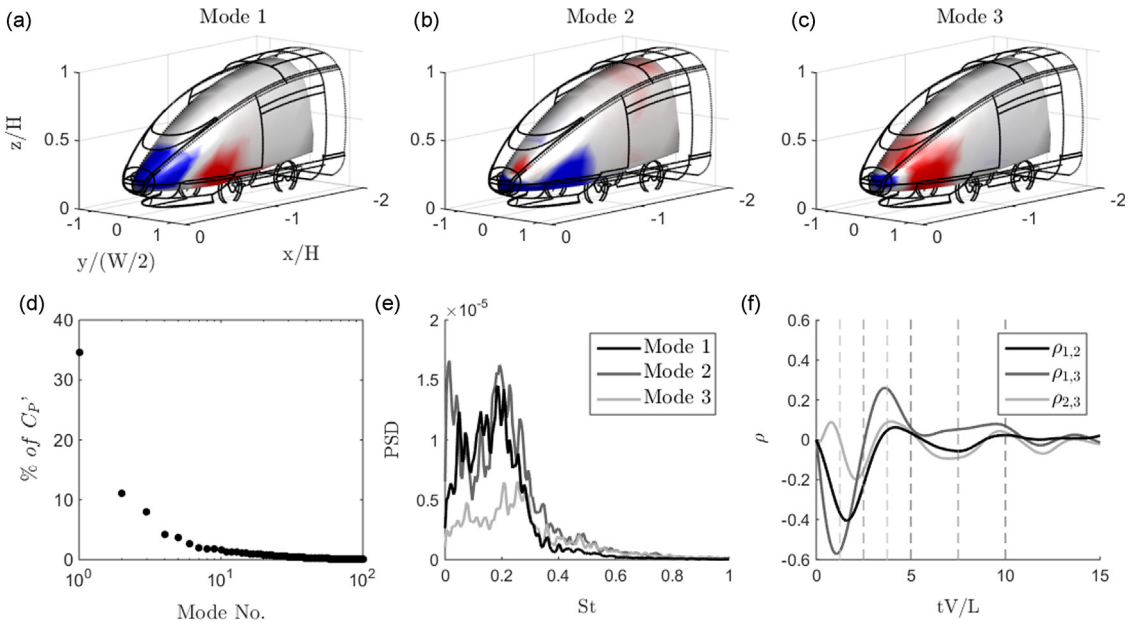

Fig. 12. Proper Orthogonal Decomposition of tail surface pressure.(a,b,c) Fluctuating POD modes 1–3 of tail surface pressure. (d) Contribution to fluctuating tail surface pressure of POD modes. (e) Power spectral density and (f) cross-correlation of modes 1–3.

contribution to pressure fluctuations as mode 2 at 9%, however, it represents a fluctuation of pressure at the tail tip. As Mode 3 is located centrally, is proposed to be associated the expected vertical shedding occurring off the tail tip.

Spectral analysis of reconstructed transient pressure using each of the 3 modes was performed on an individual point on the tail side ('tail side y+', $x=-0.61(H), y=0.81(W/2), z=0.18(H)$, in Fig. 8(d). This point was within the regions of fluctuating pressure in each of the 3 modes, and was representative of other points within these areas. The dominant frequency of St_W=0.2 in the PSD of each mode (Fig. 12(e) is clearly visible in modes 1 and 2. For mode 3, the St_W=0.2 peak exists, but together with a broader peak at St_W=0.27.

Cross-correlation of the modes to each other was also calculated (Fig. 12(f). These results show there is a very strong correlation between modes 1 and 3 ($\rho=-0.6$), and to a lesser extent 1 and 2 ($\rho=-0.4$). As the non-dimensional time period of $tV/L=5$ corresponds to the frequency of St_W=0.2, modes 1 and 3 are out-of-phase by $\approx 80^\circ$ and modes 1 and 2 by $\approx 100^\circ$. As the first 3 modes represent 55% of the total fluctuating pressure on the tail surface, they share the dominant frequency in transient surface pressure and wake measurements, and the modes show high correlation with each other, this combination of modes well represent the dominant fluctuations of pressure over the surface and corresponding dynamics of the wake.

The unsteady experimental analysis has, for the first time to the authors' knowledge, identified signs of periodicity in the surface pressure on the tail of a HST. The frequency analysis and cross-correlation of individual points, representative transient time-steps and POD analysis has identified coherent fluctuations in surface pressure that further strengthened the proposal that these arise from the vortex shedding off the vehicles side and off the tail tip.

4. Conclusions

Insight into the time-averaged and unsteady wake topology of a high-speed train has been presented.

Two dominant time-averaged features of a HST wake have been identified by 4-hole dynamic pressure probe measurements in the wake together with surface flow visualisations: a pair of counter-rotating streamwise vortices trailing the HST; and an arch vortex approaching the ballast.

In terms of the time-dependent analysis, unsteady features occurring at a dominant frequency of St_W=0.2 have been shown or inferred from time-resolved wake velocity measurements showing agreement with existing analogous literature. Analysis of the unsteadiness of the three components of velocity in the wake has shown that the streamwise vortex pair exhibits high levels of fluctuation. Further, this analysis has identified the regions of high fluctuation at St_W=0.2 occur in different positions in the wake for the different velocity components: in the streamwise vortex cores for u, in a spanwise band for v, and a central region around the tail tip for w.

As discussed in the paper, and through analogies with wakes of two-dimensional bluff bodies and automotive geometries, the unsteadiness and positioning of fluctuating v and w velocity components are consistent with an interpretation of weak spanwise (von Kármán-type) vortex shedding occurring from the sides together with lower-level vertical shedding

occurring off the tail tip. These near-wake unsteady features are tightly coupled with oscillations of the streamwise vortex pair. This common periodicity is clearly evident downstream in u velocity component fluctuations in the trailing vortex cores. Indeed, as the same dominant frequency of $St_W=0.2$ was observed in different part of the wake dominated by the different fluctuating velocity components, it is expected that the spanwise shedding, vertical shedding and periodicity of the pair of streamwise vortices constitute different components of the same dynamic flow system. However, even though these three features exist and interact coherently, in terms of physical insight it makes some sense to reconstruct a picture of the wake as consisting of these separate identifiable features, as has been pursued in this paper.

Further evidence of spanwise shedding contributing to the wake structure was observed through alternating spanwise fluctuations in the velocity along the sides but well upstream of the tail, together with measured surface pressures either side of the tail. Both exhibited 180° out-of-phase correlations.

Furthermore, transient and phase-averaged pressure displayed alternating regions of positive and negative fluctuating pressure that convect along the side surface of the tail. It is proposed this is a result of the fluctuations of pressure in the wake being transmitted upstream as vortex shedding occurs. However, the results do not rule out that the fluctuations originate upstream (perhaps from the bogies) and subsequently trigger the observed fluctuations in the wake. The high level of contribution to fluctuating surface pressure (55%) of the first 3 POD modes, each having the same dominant frequency of $St_W=0.2$, consistent with the transient surface pressures and wake velocity measurements, and having high correlation with each other, further strengthens the case that a periodic, unsteady wake topology, related to the surface pressure, exists behind a HST.

The unsteady results in the wake and over the surface of a HST ,and the correlation between these, are new experimental results. They have allowed the salient features of the unsteady HST wake to be described for the first time experimentally. The agreement with the wake structure and dynamics from the numerical literature, and the ability of the proposed flow structures to explain observed phenomena established in full-scale and scaled moving-model experiments suggest that the findings are representative of the time-averaged and unsteady wake structure and resulting slipstream around a full-scale high-speed train.

Acknowledgements

The Faculty of Engineering, Monash University is acknowledged for the Engineering Research Living Allowance stipend scholarship for J.R. Bell. The DIN Standards Railway Committee (FSF) is acknowledge for the providing the ICE3 geometry.

References

Ahmed, S.R., 1983. Influence on base slant on the wake structure and drag of road vehicles. J. Fluids Eng., Trans. ASME 105 (4), 429–434.
Baker, C.J., Dalley, S.J., Johnson, T., Quinn, A., Wright., N.G., 2001. The slipstream and wake of a high-speed train. Proc. Inst. Mech. Eng. Part F: J. Rail Rapid Transp. 215 (2), 83–99.
Baker, C., Quinn, A., Sima, M., Hoefener, L., Licciardello, R., 2012. Full scale measurement and analysis of train slipstreams and wakes: Part 1 ensemble averages. Proc. Inst. Mech. Eng. Part F: J. Rail Rapid Transp..
Baker, C.J., 2010. The flow around high speed trains. J. Wind Eng. Ind. Aerodyn. 98, 277–298.
Bearman, P.W., Beer, D.D., Hamidy, E., Harvey, J.K.(1988) The effect of a moving floor on wind-tunnel simulation of road vehicles. SAE Technical Paper No. 880245.
Bell, J.R., Burton, D., Thompson, M.C., Herbst, A.H., Sheridan, J., 2014. Wind tunnel analysis of the slipstream and wake of a high-speed train. J. Wind Eng. Ind. Aerodyn. 134, 122–138.
Bell, J.R., Burton, D., Thompson, M.C., Herbst, A.H., Sheridan, J., 2015. Moving model analysis of the slipstream ad wake of a high-speed train. J. Wind Eng. Ind. Aerodyn. 136, 127–137.
Bergh, H., Tijdeman, H., 1965. Theoretical and Experimental Results for the Dynaic Response of Pressure Measuring Systems. National Aero and Astronautical Research Institute, Amsterdam Report NLR-TRF, 328.
Castro, I.P., Robins, A.G., 1997. The flow around a surface-mounted cube in uniform and turbulent streams. J. Fluid Mech. 79 (2), 305–335.
CEN European Standard. 2009 Railway Applications-Aerodynamics Part 4: Requirements and Test Procedures for Aerodynamics on Open Track,CEN EN 14067–4.
DIN Standards Committee Railway/Normenausschuss Fahrweg und Schienenfahrzeuge (FSF),2014 ⟨www.fsf.din.de⟩.
European Rail Agency (ERA),2008, EU Technical Specification For Interoperability Relating to the Rolling Stock Sub-System of the Trans-European High-Speed Rail System (HS RST TSI), 232/EC.
Gilbert, T., Baker, C.J., Quinn, A., 2013. Gusts caused by high-speed trains in confined spaces and tunnels. J. Wind Eng. Ind. Aerodyn. 121, 39–48.
Gilhome, B.R., Saunders, J.W., Sheridan, J. Time averaged and unsteady near-wake analysis of cars. SAE Technical Paper, 2001–01–1040.
Graftieaux, L., Michard, M., Grosjean, N., 2001. Combining piv, pod and vortex identification algorithms for the study of unsteady turbulent swirling flows. Meas. Sci. Technol. 12, 1422–1429.
Graftieaux, L., Michard, M., Grosjean, N., 2001. Combining piv, pod and vortex identification algorithms for the study of unsteady turbulent swirling flows. Meas. Sci. Technol. 12, 1422–1429.
Heft, A.I., Indinger, T., Adams, N.A. Introduction of a new realistic generic car model for aerodynamic investigations. SAE Technical Paper, 2012–01–0168.
Heine D. Lauenroth G. Haff J. Huntgeburth S., Ehrenfried, K., 2013. High-speed particle image velocimetry on a moing train model, In: Proceedings of the 2nd International Symposium on Rail Aerodynamics, Berlin, Germany.
Hemida, H., Baker, C., Gao, G., 2014. The calculation of train slipstreams using large-eddy simulation. Proc. Inst. Mech. Eng. Part F: J. Rail Rapid Transp. 228 (1), 25–36.
Hooper, J.D., Musgrove, A.R., 1997. Reynolds stress, mean velocity, and dynamic static pressure measurement by a four-hole pressure probe. Exp. Therm. Fluid Sci. 15, 375–383.
Iberall, A.S., 1950. Attenuation of oscllatory pressures in intrument lines. US Department of Commerce National Bureau of Standards 45 (RP2115), 93–107.

Irwin, H.P.A.H., Cooper, K.R., Girard, R., 1979. Correction of distortion effects casued by tubing systems in measurements of fluctuating pressures. J. Ind. Aerodyn. 5, 93–107.
Jeong, J., Hussain, F., 1995. On the identification of a vortex. J. Ind. Aerodyn. 285, 69–94.
Krajnović, S., Davidson, L., 2005. Influence of floor motions in wind tunnels on the aerodynamics of road vehicles. J. Wind Eng. Ind. Aerodyn. 93, 677–696.
Kwon, H., Park, Y., Lee, D., Kim, M., 2001. Wind tunnel experiments on korean high-speed trains using various ground simulation techniques. J. Wind Eng. Ind. Aerodyn. 89, 1179–1195.
Lödgberg, O., Fransson, J.H.M., Alfredsson, P.H., 2009. Streamwise evolution of longitudinal vortices in a turbulent boundary layer. J. Fluid Mech. 623.
Lienhart, H., Pêgo, J.P. Spectral density and time scales of velocity flutuations in the wake of a simplified car model. SAE Technical Paper, 2012–01–0592.
Lumley, J.L., 1967. The structure of inhomogeneous turbulent flows. In: Yaglom, A.M., Tatarski, V.I. (Eds.), Atmospheric Turbulence and Radio Wave Propagation, pp. 166–178.
Minguez, M., Pasquetti, R., Serre, E., 2008. High-order large-eddy simulation of flow over the ahmed body car model. Phys. Fluids 20, 095101.
Morel, T., 1980. Effect of base slant on flow in the near wake of an axisymmetric cylinder. Aeronaut. Q., 132–147.
Morton, B.R., 1984. The generation and decay of vorticity. Geophys. Astrophys. Fluid Dyn. 28, 277–293.
Morton, B.R., 1987. Trailing vortices in the waks of surface-mounted obstacles. J. Fluid Mech. 175, 247–293.
Muld, T., Efraimsson, G., Hennigson, D.S., 2012. Mode decomposition on surface-mounted cube. Flow, Turbul. Combust. 88, 279–310.
Muld, T., Efraimsson, G., Hennigson, D.S., 2012. Flow structures around a high-speed train extracted using proper orthogonal decomposition and dynamic mode decomposition. Proc. Inst. Mech. Eng. Part F: J. Rail Rapid Transp. 57, 87–97.
Muld, T., Efraimsson, G., Hennigson, D.S., 2012. Mode decomposition and slipstream velocities in the wake of two high-speed trains. Int.J. Railw. Technol. (submitted for publication). Submitted.
Muld, T., Efraimsson, G., Hennigson, D.S., 2013. Wake characteristics of high-speed trains with different lengths. Proc. Inst. Mech. Eng.Part F: J. Rail Rapid Transp.. http://dx.doi.org/10.1177/0954409712473922.
Pauley, W.R., Eaton, J.K., 1988. Experimental studey of the development of longitudinal vortex pairs embedded in a turbulent boundary layer. AIAA J. 26 (7), 816–823.
Perrin, R., Braza, M., Cid, E., Cazin, S., Barthet, A., Sevrain, A., Mockett, C., Thiele, F., 2007. Obtaining phase averaged turbulence properties in the near wake of a circular cylinder at high reynolds number using pod. Exp. in Fluids 43, 341–355.
Pii, L., Vanoli, E., Polidoro, F., Gautier, S., Tabbal, A., 2014. Aa full scale simulation of a high speed train for slipstream prediction. Pro. Transp. Res. Arena, Paris, France.
Pope, C.W., 2007. Effective management of risk from slipstream effects at trackside and platforms. Rail Safety and Standards Board - T425 Report.
Provansal, M., Mathis, C., Boyer, L., 1987. Bénard-von kármán instability: transient and forced regimes. J. Fluid Mech. 182, 1–22.
Roshko, A., 1955. On the wake and drag of bluff bodies. J. Aeronaut. Sci. 22, 124–132.
Schober, M., Weise, M., Orellano, A., Deeg, P., Wetzel, W., 2010. Wind tunnel investigation of an ice3 endcar on three standard ground scenarios. J. Wind Eng. Ind. Aerodyn. 98, 345–352.
Schulte-Werning, B., Heine, B., Matschke, C., 2001. Slipstream development and wake flow characteristics of modern high-speed trains. J. Appl. Math. Mech. 81 (S3), 789–790.
Schulte-Werning, B., Heine, B., Matschke, C., 2003. Unsteady wake flow characteristics of high-speed trains. Proc. Appl. Maths Mech. 2, 332–333.
Sirovich, L., 1987. Turbulence and the dynamics of coherent structures part i: Coherent structures. Q. Appl. Math. 45 (3), 561–590.
Strachan, R.K., Knowles, K., Lawson, N.J., 2007. The vortex strucutre behind an agmed refernce model in the presence of a moving ground plane. Exp. Fluids 42, 659–669.
Vino, G., Watkins, S., Mousley, P., Watmuff, J., Prasad, S., 2005. Flow structures in the near-wake of the ahmed model. J. Fluids Struct. 20, 673–695.
Wang, X.W., Zhou, Y., Pin, Y.F., Chan, T.L., 2013. Turbulent near wake of an ahmed vehicle model. Exp. Fluids 54, 1490.
Weise, M., Schober, M., Orellano A. (2006) Slipstream velocities induced by trains. Proceedings of the WSEAS International Conference on Fluid Mechanics and Aerodynamics, Elounda, Greece.
Westphal, R.V., Mehta, R.D., 1989. Interaction of an oscillating vortex with a turbulent boundary layer. Exp. Fluids 7, 405–411.
Yao, S., Sun, Z., Guo, D., Chen, D., Yang, G., 2013. Numerical study on wake characteristics of high-speed trains. Acta Mech. Sin. 29 (6), 811–822.